Short Communication

Laser additive manufacturing of a carbon-supersaturated β-Ti alloy for biomaterial application

Mingqi Dong [a], Yu Zhang [a], Weiwei Zhou [a], Peng Chen [b], Zhenxing Zhou [a], Hiroyasu Kanetaka [b], Takuya Ishimoto [c,d], Yuichiro Koizumi [d,e], Takayoshi Nakano [d,e], Naoyuki Nomura [a,*]

[a] Department of Materials Processing, Graduate School of Engineering, Tohoku University, Sendai, 980-8579, Japan
[b] Division of Interdisciplinary Co-Creation (ICC-Division), Liaison Center for Innovative Dentistry, Graduate School of Dentistry, Tohoku University, Sendai, 980-8575, Japan
[c] Aluminium Research Center, University of Toyama, 3190, Gofuku, Toyama 930-8555, Japan
[d] Division of Materials and Manufacturing Science, Graduate School of Engineering, Osaka University, 2-1 Yamadaoka, Suita, Osaka 565-0871, Japan
[e] Anisotropic Design and Additive Manufacturing Research Center, Osaka University, 2-1 Yamadaoka, Suita, Osaka 565-0871, Japan

A R T I C L E   I N F O

A B S T R A C T

Developing high-performance β-Ti alloys is a persistent and long-term demand for the advancement of next-generation biomaterials. In this study, a strategy of leveraging the unique characteristics of laser powder bed fusion (L-PBF) technique and nanocarbon materials was proposed to design a novel carbon-supersaturated β-Ti alloy. Ultrathin graphene oxide (GO) sheets were closely covering onto spherical Ti-15Mo-5Zr-3Al (Ti1553) powders, enhancing laser absorptivity while maintaining good flowability. Consequently, the GO-added Ti1553 builds tended to be denser than the initial ones, indicating an improved additive manufacturability. During L-PBF, GO sheets were completely dissolved into the Ti1553 matrix, generating fully carbon-supersaturated β-Ti structures with a reduced grain size. Thanks to the exceptional strengthening effects of high-concentration solid-solution carbon (~0.05 wt%), the GO/Ti1553 builds achieved a high ultimate tensile strength of 1166 MPa. Moreover, as revealed by the immunofluorescence staining experiments, the GO/Ti1553 builds demonstrated a retained cytocompatibility. This study provides new insight into composition and processing design of high-performance Ti components for biomedical applications.

1. Introduction

Owing to their high specific strength, good corrosion resistance and excellent biocompatibility, titanium and its alloys have been widely used in the biomedical and healthcare industry [1]. Considering the large mismatch of Young's modulus between nature bone (10–30 GPa) [2] and Ti implants (~105 GPa) [3], the development of high-strength, low Young's modulus Ti-based materials has been an enduring topic. β-Ti alloys exhibit a significant drop in Young's modulus (e.g., reaching values as low as approximately 36 GPa [4]), making them promising candidates for next-generation biomaterials to replace hard human tissues. Although there is a common trade-off between strength and ductility in Ti alloys, an increase in strength while maintaining adequate elongation (~10–25 %) is preferred for enhanced reliability [5]. Improving the mechanical properties of Ti-based materials has often been attempted by adding reinforcement particles (e.g., ceramics or nanocarbon materials) to generate titanium matrix composites (TMCs) [6,7], or by doping with light elements such as nitrogen and oxygen [8]. These novel materials are primarily developed via casting or powder metallurgy. Unfortunately, the traditional methods typically result in coarse reinforcements and microstructure heterogeneity [6], as well as significant segregation of light elements within the matrix [9], which hinders the mechanical performance of Ti-based materials.

Laser powder bed fusion (L-PBF), as a form of additive manufacturing technology, has garnered increasing attention for fabrication Ti-based materials owing to its ability to directly produce net-shape structures with high geometric complexities [10]. This technique has demonstrated advantages in creating β-Ti alloys with a lattice structure, which exhibit significantly improved impact resistance [11]. Apart from its capability for freeform fabrication, L-PBF is anticipated as a synthesis technique for producing high-performance metallic components using pre-alloyed powders or composite powders [12]. The

---

* Corresponding author.
  E-mail addresses: weiwei.zhou.c3@tohoku.ac.jp (W. Zhou), naoyuki.nomura.a2@tohoku.ac.jp (N. Nomura).

ultrahigh processing temperature, large cooling rate ($\sim 10^3$–10^8 Ks^{-1}), and large thermal gradient in the molten pools contribute to the development of non-equilibrium phases, novel microstructures, and enhanced performance in L-PBF products [13-17]. For example, controlling the crystallographic texture of Ti-15Mo-5Zr-3Al (Ti1553) alloy through L-PBF has been confirmed to successfully reduce the Young's modulus to 68.7 GPa [18-20], demonstrating the significant potential of L-PBF in developing novel materials.

Using Ti1553 as a model material, this study proposes a strategy that leverages the unique characteristics of L-PBF process and nanocarbon material, specifically graphene oxide (GO), to design high-performance β-Ti alloys. GO has recently been applied in developing Ti implants as a surface coating material to enhance osseointegration and corrosion resistance in orthopedic applications [21,22]. It has also been used as an additive in Ti alloys due to its excellent mechanical properties and ability to form TiC reinforcing particles during high-temperature processing [23,24]. Beyond these promising applications, GO is highly anticipated as a filler material for synthesizing novel Ti alloys via L-PBF due to its intrinsic features. The presence of abundant surface functional groups facilitates the production of uniform composite powders through an electrostatic self-assembly during a hetero-agglomeration process. The ultralow thickness and flexibility of GO enables the GO-decorated metallic powders to retain their original morphology and particle size, thus improving the L-PBF processability of Ti1553 alloy [25]. Furthermore, owing to the ultrahigh processing temperature and rapid solidification of L-PBF process, as well as the large specific surface area of GO, the decomposition of GO may occur under laser irradiation, resulting in high-concentration doping of elemental C/O into the matrix and thus enhancing the mechanical performance. In this study, the effects of GO decoration on the powder properties, L-PBF processability, and microstructure evolution, mechanical performance and cytocompatibility of Ti1553 alloy will be firstly clarified.

2. Material and methods

Starting Ti1553 alloy powders (OSAKA Titanium Technologies Co. Ltd., Japan) were produced by gas atomization. Aqueous GO colloid with a concentration of 1 wt% was received from Nippon Shokubai Company Limited., Japan. The GO sheets exhibited an average lateral size of $\sim$1 μm and an average thickness of $\sim$1.5 nm. A 0.2 wt% GO/Ti1553 composite powder was prepared through the hetero-agglomeration process as described in previous study [15]. Ti1553 and GO/Ti1553 bulk specimens were fabricated using a commercial laser cusing system (Concept Laser MlabR, Germany) equipped with an ytterbium fiber laser with the wavelength of 1070 nm. The L-PBF build quality is primarily determined by the output energy density (E), which can be expressed as [26]:

$$E = \frac{P}{vth}$$

where P is the laser power, v is the laser scanning speed, t is the layer thickness, and h is the hatch distance. Various energy densities, corresponding to different processing parameters (see Table S1), were utilized to obtain the L-PBF builds. A typical "chess pattern" [27] was applied as scanning strategy for all build fabrications. The whole building process was carried out in an argon atmosphere with a low oxygen concentration of <0.1 %.

The particle size distributions of Ti1553 and GO/Ti1553 powders were evaluated via a laser diffraction particle size analyzer (HELOS/RODOS, Sympatec GmbH, Germany). The powder flowability was measured by a revolution method (REVOLUTION Powder Analyzer, Mercury Scientific Inc., USA). The apparent density and tap density of powders were measured according to ASTM B417–18 and ASTM B527 –15, respectively. The Hausner ratio (HR) was calculated as the ratio of the tap density to the apparent density as:

$$HR = \frac{\rho_T}{\rho_A}$$

where ρ_T is the tap density, ρ_A is the apparent density. The laser absorptivity of powders was measured by a UV–VIS–NIR spectrometer (V-670, JASCO, Japan). The apparent densities of L-PBF builds were evaluated by the Archimedes' principle. The phase constitution was analyzed via X-ray diffraction (XRD) using a diffractometer (SmartLab 9 kW, Rigaku, Japan). The microstructural characterizations were carried out using a field emission scanning electron microscope (FESEM; JSM-6500F, JEOL, Japan), electron probe microanalysis (EPMA; JXA-8530F, JEOL, Japan), transmission electron microscope (TEM; JEM-2100F, JEOL, Japan), scanning TEM (STEM; JEM-ARM200F, JEOL, Japan), and electron back-scattered diffraction (EBSD) set up inside a FESEM (JSM-7100F, JEOL, Japan). The carbon contents of L-PBF builds were determined by combustion analysis (CS844, LECO Co., Ltd., USA). Vickers hardnesses of L-PBF builds were evaluated using a hardness test machine (HM-200, Mitutoyo, Japan) with a peak load of 0.98 N and a holding time of 10 s. Uniaxial tensile tests were conducted on a universal testing machine (INSTRON 5892, US) at room temperature with an initial strain rate of $1 \times 10^{-3} \, s^{-1}$. The tensile loading direction is perpendicular to the building direction of the L-PBF process. The dog-bone-shaped specimens were machined from the L-PBF builds with a gauge length, width, and thickness of 10 mm, 2 mm, 1.5 mm, respectively. The nominal strain was measured using foil strain gauges (KFGS-4N-120-C1–11, KYOWA, Japan) attached to the surface of tensile specimens. The Young's moduli of L-PBF builds were calculated from the elastic deformation region of the obtained tensile stress-strain curves. Both the Ti1553 and the GO/Ti1553 builds were tested three times. The biocompatibility of dense L-PBF builds was evaluated by a visualization of cell initial adhesion through immunofluorescence staining. The detailed experimental procedures and characterization methods can be found in Supplementary Information (see Supplementary Note 1).

3. Results and discussion

3.1. Effects of nanocarbon addition on powder properties and additive manufacturability

The morphologies of Ti1553 powder and GO/Ti1553 composite powder were shown in Fig. 1a and b. As indicated by the red arrows, the GO sheets were attached to the surface of Ti1553 powder without apparent agglomeration. Due to the ultrathin dimension ($\sim$1.5 nm) and high flexibility features of GO sheets, the composite powders remained almost the same powder size distribution to the Ti1553 powder with a medium particle size (D_{50}) of 32.2 μm (Fig. 1c).

Powder bed quality and laser absorptivity are generally considered as two critical factors determining the L-PBF processability of powders. Uniform powder bed with high packing density can be achieved at a high powder flowability. The flowability was quantitatively evaluated by measuring avalanche angles during particle revolution tests. There was no significant difference between the avalanche angles of the Ti1553 (43.4°) and the GO/Ti1553 (43.1°) powders, indicating an unchanged powder bed flowability after GO addition. This result was mainly attributed to the remained powder morphology and particle size distribution of the composite powder (Fig. 1a-c). The Hausner ratios of Ti1553 and GO/Ti1553 powders were respectively determined as 1.11 and 1.03 (Table S2), indicating similar compressibility. Moreover, owing to the high laser absorptivity of GO sheets (87.5 %), the laser absorptivity of Ti1553 powder bed significantly increased from 69.8 % to 77.6 % at the laser wavelength of 1070 nm utilized in L-PBF (Fig. 1d). Therefore, the GO/Ti1553 powder showed unchanged powder bed quality and improved laser absorptivity, which is expected to improve the laser additive manufacturability.

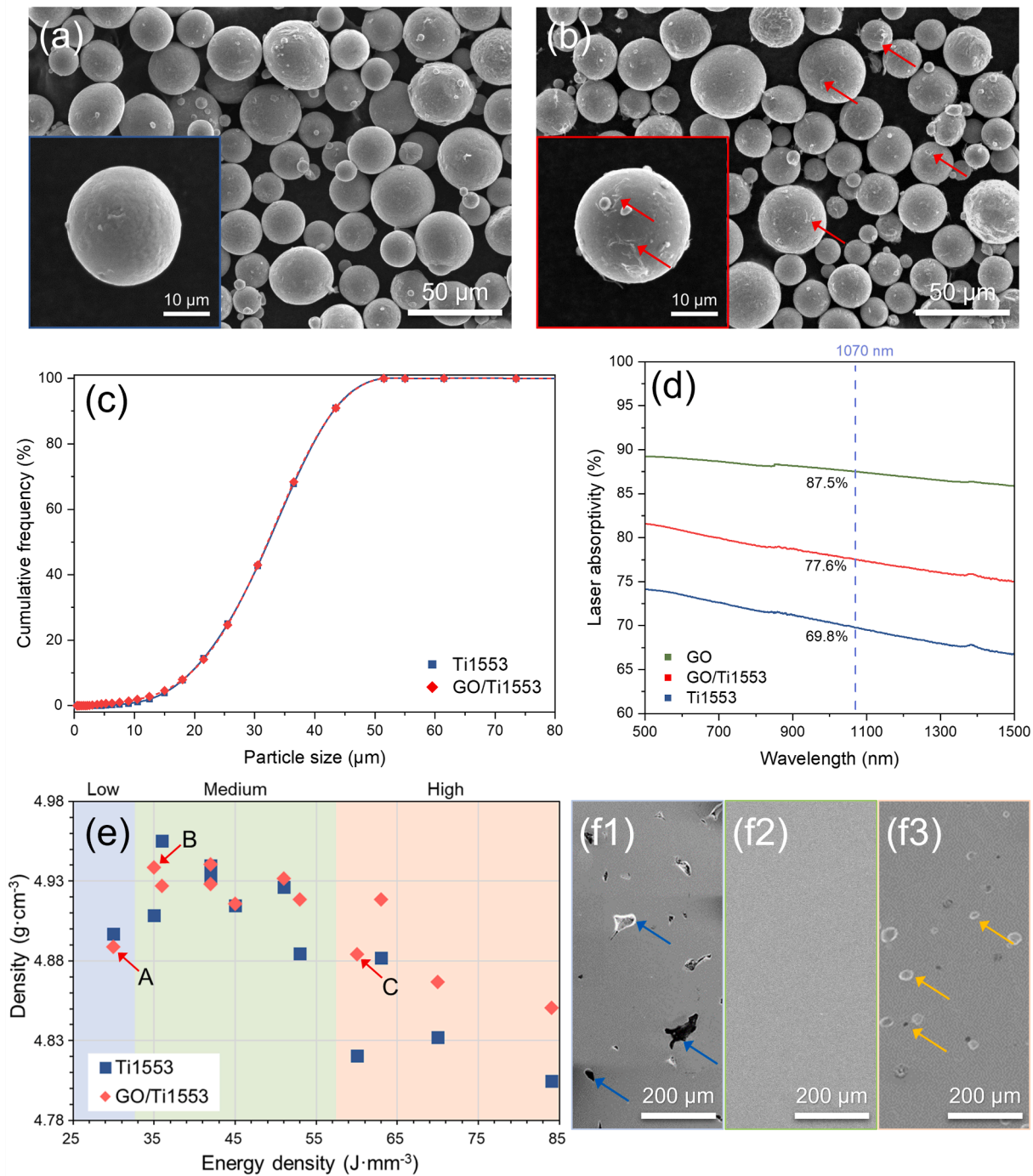The effects of nanocarbon addition on the melting behavior of

Fig. 1. FESEM images of (a) Ti1553 powder and (b) GO/Ti1553 powder; (c) particle size distribution of Ti1553 and GO/Ti1553 powder; (d) laser absorptivity of GO, GO/Ti1553, and Ti1553 powders as a function of laser wavelength; (e) density distribution of Ti1553 and GO/Ti1553 builds as a function of output energy density; cross-sectional morphologies of GO/Ti1553 builds with the energy densities corresponding to the (f1) A, (f2) B, and (f3) C points in Fig. 1e.

Ti1553 powders were investigated by L-PBF builds evaluation. Fig. 1e indicated the densities of both Ti1553 and GO/Ti1553 builds as a function of the output energy density (E). Similar to the Ti1553 alloy, the density of GO/Ti1553 builds firstly increased, then subsequently decreased with the increase of E. Figs. f1-f3 indicated the corresponding cross-section morphology of GO/Ti1553 builds. When a low E was applied (blue area in Fig. 1e), large irregular-shaped pores (arrows in Fig. f1) were observed in the build, being recognized as lack-of-fusion defects caused by insufficient fusion of powders [28]. In contrast, when a high E was applied (orange area in Fig. 1e), spherical pores with

size of tens of micrometers (arrows in Fig. f3) were detected in the builds, corresponding to keyhole pores formed by the melt evaporation during laser irradiation [29]. In addition, there were no obvious defects detected in the samples fabricated using medium E (green area in Fig. 1e), showing a high build density of >4.95 g·cm^{-3}. In general, the average density (~ 4.91 g·cm^{-3}) of the GO/Ti1553 builds tended to be higher than that of the Ti1553 builds (~ 4.89 g·cm^{-3}), attributing to the improved powder bed quality and laser absorptivity by nanocarbon addition. Interestingly, the GO/Ti1553 builds were obviously denser than the Ti1553 builds at high E area. This result can be attributed to the

modified surface tension of melts induced by C/O solution from GO, restricting the formation of keyholes during L-PBF [25]. The optimized building parameters, with a scanning speed of 1000 mm·s^{-1} and hatch distance of 105 μm for Ti1553, and a scanning speed of 1200 mm·s^{-1} and hatch distance of 75 μm for GO/Ti1553, produced the L-PBF builds with the highest densities. These builds were subsequently used for further characterization.

3.2. Effects of nanocarbon addition on the microstructure evolution and mechanical response of Ti1553

The effects of nanocarbon addition on the microstructure and mechanical properties of Ti1553 alloy were revealed. The phase constitution of L-PBF builds was determined by XRD analysis. As indicated in Fig. 2a, both the Ti1553 and GO/Ti1553 builds were composed of body-centered cubic (bcc) structure, corresponding to β-Ti phase. Fig. 2b and c show the cross-sectional microstructure of the Ti1553 and GO/Ti1553 builds parallel to the building direction (BD). As indicated by the dot lines, large-scale traces approximately half-elliptical in shape were clearly observed in two samples, which were identified as the boundaries of molten pools.

Fig. 2d shows the EPMA mappings of the GO/Ti1553 build. All the elements distributed in the matrix homogeneously without significant micro-segregation. Fig. 2e and f show the TEM images and corresponding SAED patterns of the Ti1553 and GO/Ti1553 builds, respectively. Both samples were merely composed of β-Ti phase. No nanoprecipitates or residual GO sheets were detected in the GO/Ti1553 build by careful TEM observations. The close-up STEM observation and

energy dispersive X-ray spectroscopy (EDS) mappings in Fig. S1 also confirmed the homogeneous distribution of alloying elements, including carbon and oxygen. These results were in good agreement with the XRD analysis and FESEM observations. According to the high-temperature combustion analysis, the carbon content of the GO/Ti1553 build was determined as 0.050 wt%, which was much higher than that of the Ti1553 build (0.004 wt%) and the carbon solubility of β-Ti (~0.006 wt %) [30]. Moreover, the oxygen content of the Ti1553 build increased from 0.153 to 0.231 wt% due to the surface oxygen-containing groups of GO. Based on the above, it is thought that the GO sheets were completely dissolved into the Ti1553 matrix during L-PBF process, attributing to the reduced thermal stability of defective GO sheets under laser irradiation [31]. Due to the rapid cooling of L-PBF, such a novel C-supersaturated β-Ti alloy has been firstly fabricated in this work. Compared with traditional processing methods, L-PBF technique exhibited intrinsic advantages of fabricating nonequilibrium, uniform structures [32,33].

The impact of supersaturated carbon on the metallurgy phenomenon of Ti1553 was further investigated by EBSD analysis. Fig. 2g and h display the inverse pole figure (IPF) images of the Ti1553 and GO/Ti1553 builds. Insignificant change was detected in the crystallographic texture of the builds; however, there was a reduction in the average grain size from 41.7 μm to 29.5 μm induced by adding carbon. The grain refinement was primarily attributed to the solid solution of C/O atoms, which are typically classified as light elements known to have a grain-refining effect.

The mechanical properties of the L-PBF builds were evaluated by Vickers hardness and tensile tests. The Vickers hardness of the Ti1553 build increased from 290 to 331 HV (Fig. 3a) by GO addition. As
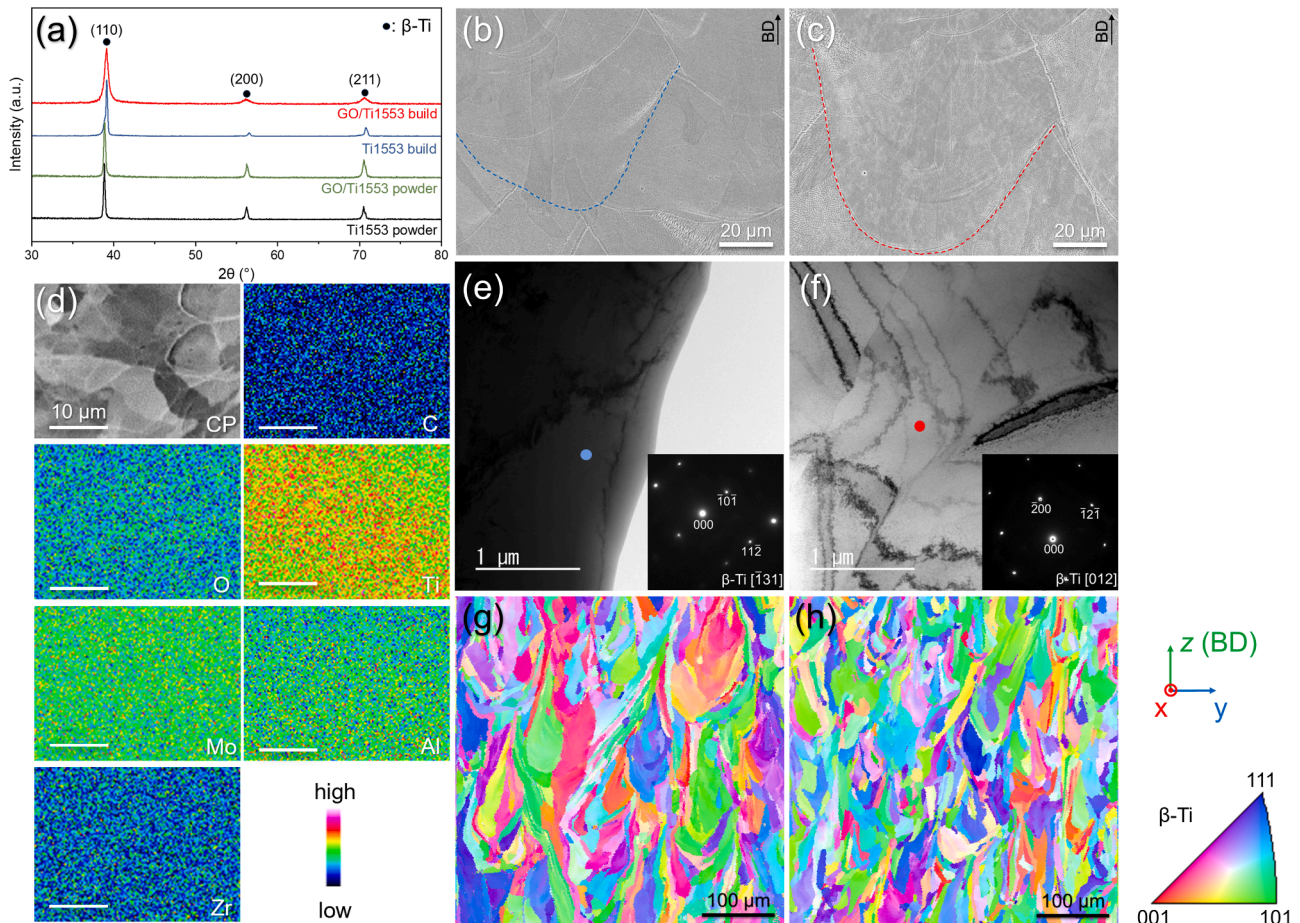

Fig. 2. (a) XRD patterns of the Ti1553 powder, GO/Ti1553 powder, Ti1553 build, and GO/Ti1553 build; FESEM images of the (b) Ti1553 and (c) GO/Ti1553 builds; (d) EPMA mappings of the GO/Ti1553 build; TEM images of the (e) Ti1553 and (f) GO/Ti1553 builds; EBSD-IPF images of the cross-sectional (g) Ti1553 and (h) GO/ Ti1553 builds along the building direction. Inserts in (e, f) show the corresponding SAED patterns taken from the (e) bule and (f) red spots, respectively.
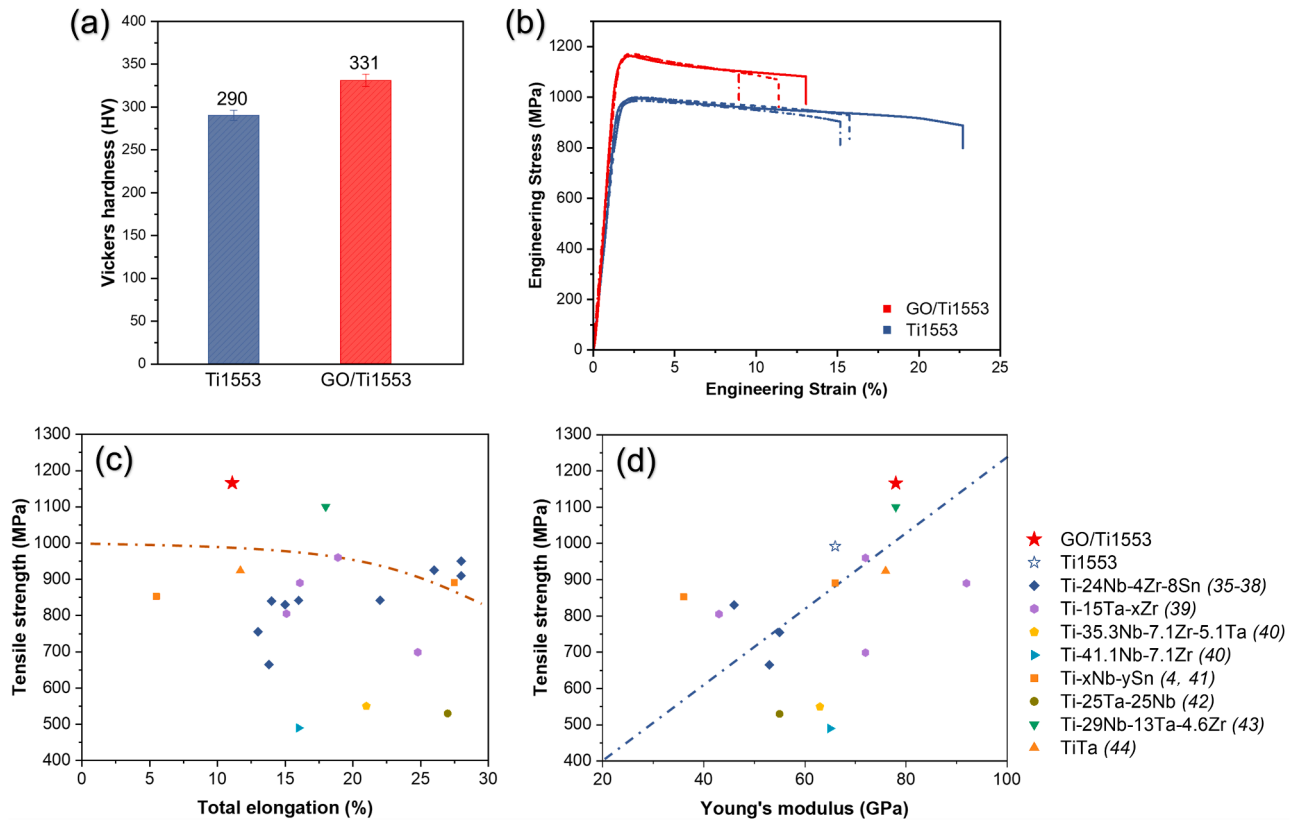
Fig. 3. (a) Vickers hardness and (b) tensile stress-strain curves of the Ti1553 and GO/Ti1553 builds; tensile strength as a function of (c) elongation and (d) Young's modulus of the GO/Ti1553 build as compared with previously reported β-type Ti alloys fabricated by conventional methods and additive manufacturing. The dashed lines in (c, d) indicate the trend in the distribution of mechanical properties as the variables change.

displayed in Fig. 3b, the average yield strength (YS) and ultimate tensile strength (UTS) of the Ti1553 alloy build was determined as 950 and 992 MPa, respectively. While the YS and UTS of the GO/Ti1553 build increased to 1121 and 1166 MPa, respectively, simultaneously displaying an 18 % enhancement. Meanwhile, the GO/Ti1553 build retained a high ductility of 11.1 %. The Young's modulus of the Ti1553 build increased from 66.3 to 78.5 GPa through incorporating GO, attributing to the solid solution of C/O atoms [34].

As summarized in Fig. 3c and d, the GO/Ti1553 build exhibited a highest UTS while retaining a low Young's modulus compared to the β-type Ti alloys for biomedical applications reported to date [4,35-44]. Such minor addition of GO led to the remarkable enhancement of mechanical property of Ti1553, indicating the excellent strengthening behavior of nanocarbons. In addition, lower Young's modulus is further expected by controlling the texture formation through adjusting the laser scanning strategies, or by fabricating porous structures, as reported in previous studies [18,45,46]. The limited mechanical properties caused by elemental segregation and microstructure heterogeneity in conventionally fabricated Ti alloys were significantly improved by the combination of minor carbon addition and the L-PBF process.

3.3. Effects of nanocarbon addition on osteoblast behavior of L-PBF builds

It is argued that the carbides-added metallic biomaterials are relatively more bioinert than the starting metals [47]. To evaluate the potential effects of the GO addition to Ti1553 builds on the adhesion behavior of osteoblast in vitro, the cellular initial adhesion morphologies on both Ti1553 and GO/Ti1553 builds were visualized by immunocytochemistry (Fig. 4a). A similar cellular extension was observed in cells attached on both Ti1553 builds and GO/Ti1553 builds. Through

evaluating the numbers of DAPI stained nucleus (Fig. 4b), it is noted that there was no significant difference in the attached cell numbers between both the Ti1553 builds with and without GO addition. This result indicated that solid-solution of C atoms did not affect the attached cell number after 24 h incubation. The Ti1553 and GO/Ti1553 builds showed a similar good biocompatibility for cellular attachment.

4. Conclusion

In summary, a novel C-supersaturated β-Ti alloy was synthesized by L-PBF processing of minor GO-coated Ti1553 alloy powders via the hetero-agglomeration process. The ultrathin GO sheets were fitted and tightly covered onto the spherical Ti1553 powders, leading to an enhanced laser absorptivity while unchanged powder morphology and flowability. As a result, the GO/Ti1553 builds showed higher average density than the Ti1553 builds, indicating an improved additive manufacturability by GO addition. Detailed microstructural characterizations revealed that GO sheets were completely dissolved into the Ti1553 matrix after L-PBF, generating fully β-Ti structures with a decreased grain size. Thanks to the excellent strengthening effect of high-concentration solid-solution C atoms (~0.05 wt%), the UTS of GO/Ti1553 build reached to 1166 MPa, displaying an 18 % enhancement as compared with that of the Ti1553 build (992 MPa). Moreover, the immunofluorescence staining experiments revealed a similar number of initially attached cells between the Ti1553 and GO/Ti1553 specimens after 24 h incubation, suggesting that the GO/Ti1553 build retained a good cytocompatibility. This study benefits to the production of novel additive manufacturing metallic components for biomedical applications.
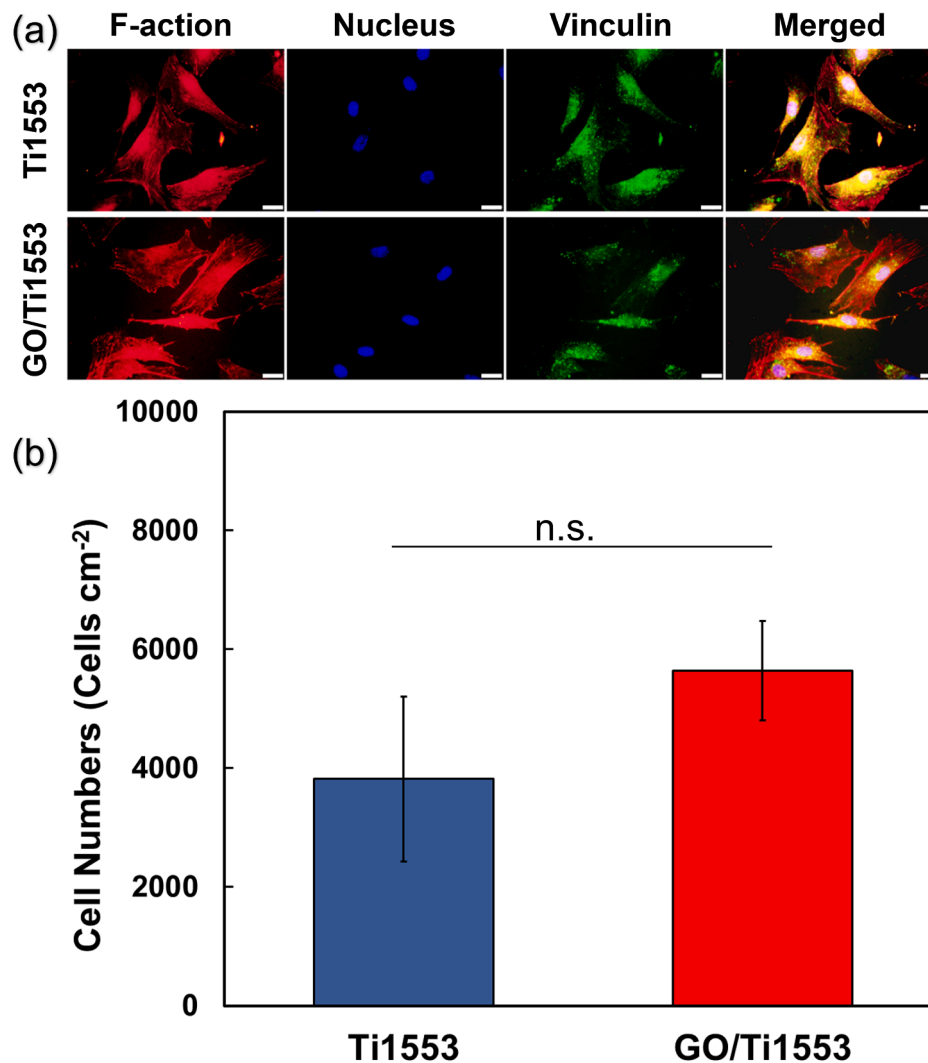
Fig. 4. (a) Morphology and (b) numbers of MC3T3-E1 cells attached to Ti1553 and GO/Ti1553 builds after 24 h of incubation. Cellular initial attachment was examined by immunofluorescent staining, where F-actin (red)-, nuclei (blue)- and vinculin (green)-positive adhesion plaques were visualized. Results were statistically analyzed. Scale bar in (a), 20 μm. n.s., non-significant.

CRediT authorship contribution statement

Mingqi Dong: Writing – original draft, Methodology, Investigation, Conceptualization. **Yu Zhang:** Methodology, Investigation. **Weiwei Zhou:** Writing – review & editing, Supervision, Funding acquisition, Conceptualization. **Peng Chen:** Writing – review & editing, Methodology, Investigation. **Zhenxing Zhou:** Investigation. **Hiroyasu Kanetaka:** Supervision. **Takuya Ishimoto:** Writing – review & editing, Resources. **Yuichiro Koizumi:** Writing – review & editing, Resources. **Takayoshi Nakano:** Writing – review & editing, Resources. **Naoyuki Nomura:** Writing – review & editing, Supervision, Project administration.

Declaration of competing interest

The authors declare that they have no known competing financial interests or personal relationships that could have appeared to influence the work reported in this paper.

Data availability

Data will be made available on request.

Supplementary materials

Supplementary material associated with this article can be found, in the online version, at doi:10.1016/j.addlet.2024.100233.

References

[1] S.S. Sidhu, et al., A review on alloy design, biological response, and strengthening of β-titanium alloys as biomaterials, Mater. Sci. Eng. C 121 (2021) 111661, https://doi.org/10.1016/j.msec.2020.111661.

[2] J.-Y. Rho, et al., Elastic properties of human cortical and trabecular lamellar bone measured by nanoindentation, Biomaterials 18 (20) (1997) 1325–1330, https://doi.org/10.1016/S0142-9612(97)00073-2.

[3] H. Liu, et al., β-Type titanium alloys for spinal fixation surgery with high Young's modulus variability and good mechanical properties, Acta Biomater 24 (2015) 361–369, https://doi.org/10.1016/j.actbio.2015.06.022.

[4] S. Guo, et al., Design and fabrication of a metastable β-type titanium alloy with ultralow elastic modulus and high strength, Sci. Rep. 5 (1) (2015) 14688, https://doi.org/10.1038/srep14688.

[5] L.-C. Zhang, J. Wang, Stabilizing 3D-printed metal alloys, Science 383 (6683) (2024) 586–587, https://doi.org/10.1126/science.adn6566.

[6] M.D. Hayat, et al., Titanium metal matrix composites: an overview, Compos. Part A Appl. Sci. Manuf. 121 (2019) 418–438, https://doi.org/10.1016/j.compositesa.2019.04.005.

[7] A. Issariyapat, et al., Solute-induced near-isotropic performance of laser powder bed fusion manufactured pure titanium, Addit. Manuf. 56 (2023) 102907, https://doi.org/10.1016/j.addma.2022.102907.

[8] T. Song, et al., Strong and ductile titanium–oxygen–iron alloys by additive manufacturing, Nature 618 (7963) (2023) 63–68, https://doi.org/10.1038/s41586-023-05952-6.

[9] K. Kondoh, et al., Tensile property enhancement by oxygen solutes in selectively laser melted titanium materials fabricated from pre-mixed pure Ti and TiO$_2$ powder, Mater. Sci. Eng. A 795 (2020) 139983, https://doi.org/10.1016/j.msea.2020.139983.

[10] S. Liu, Y.C. Shin, Additive manufacturing of Ti6Al4V alloy: a review, Mater. Des. 164 (2019) 107552, https://doi.org/10.1016/j.matdes.2018.107552.

[11] Z.-Y. Wu, et al., Microstructure and mechanical behavior of rhombic dodecahedron-structured porous β-Ti composites fabricated via laser powder bed fusion, J. Mater. Res. Technol. 31 (2024) 298–310, https://doi.org/10.1016/j.jmrt.2024.06.077.

[12] J. Wang, et al., Microstructural homogeneity and mechanical behavior of a selective laser melted Ti-35Nb alloy produced from an elemental powder mixture, J. Mater. Sci. Technol. 61 (2021) (2021) 221–233, https://doi.org/10.1016/j.jmst.2020.05.052.

[13] M. Das, et al., Laser processing of SiC-particle-reinforced coating on titanium, Scripta Mater 63 (4) (2010) 438–441, https://doi.org/10.1016/j.scriptamat.2010.04.044.

[14] P. Köhnen, et al., Understanding the process-microstructure correlations for tailoring the mechanical properties of L-PBF produced austenitic advanced high strength steel, Addit. Manuf. 30 (2019) 100914, https://doi.org/10.1016/j.addma.2019.100914.

[15] S. Sui, et al., Study of the intrinsic mechanisms of nickel additive for grain refinement and strength enhancement of laser aided additively manufactured Ti–6Al–4V, Int. J. Extrem. Manuf. 4 (3) (2022) 035102, https://doi.org/10.1088/2631-7990/ac6b61.

[16] W. Chen, et al., Compressive mechanical properties and shape memory effect of NiTi gradient lattice structures fabricated by laser powder bed fusion, Int. J. Extrem. Manuf. 4 (4) (2022) 045002, https://doi.org/10.1088/2631-7990/ac8ef3.

[17] S. Wei, et al., Laser powder bed fusion additive manufacturing of NiTi shape memory alloys: a review, Int. J. Extrem. Manuf. 5 (3) (2023) 032001, https://doi.org/10.1088/2631-7990/acc7d9.

[18] T. Ishimoto, et al., Crystallographic texture control of beta-type Ti–15Mo–5Zr–3Al alloy by selective laser melting for the development of novel implants with a biocompatible low Young's modulus, Scripta Mater 132 (2017) 34–38, https://doi.org/10.1016/j.scriptamat.2016.12.038.

[19] S.-H. Sun, et al., Comparison of microstructure, crystallographic texture, and mechanical properties in Ti–15Mo–5Zr–3Al alloys fabricated via electron and laser beam powder bed fusion technologies, Addit. Manuf. 47 (2021) 102329, https://doi.org/10.1016/j.addma.2021.102329.

[20] S.-W. Ge, et al., The effect of secondary phase on corrosion behaviors of the titanium–zirconium–molybdenum alloy, Tungsten 6 (2) (2023) 342–354, https://doi.org/10.1007/s42864-023-00228-y.

[21] H. Asgar, et al., Functionalized graphene oxide coating on Ti6Al4V alloy for improved biocompatibility and corrosion resistance, Mater. Sci. Eng. C 94 (2019) 920–928, https://doi.org/10.1016/j.msec.2018.10.046.

[22] C. Wang, et al., Enhanced osseointegration of titanium alloy implants with laser microgrooved surfaces and graphene oxide coating, ACS Appl. Mater. Interfaces 11 (43) (2019) 39470–39483, https://doi.org/10.1021/acsami.9b12733.

[23] H. Chen, et al., Excellent high-temperature strength and ductility of graphene oxide reinforced high-temperature titanium alloy matrix composite fabricated by hot isostatic pressing and heat treatment, Compos. Commun. 30 (2022) 101077, https://doi.org/10.1016/j.coco.2022.101077.

[24] Q. Yan, et al., Super-high-strength graphene/titanium composites fabricated by selective laser melting, Carbon N Y 174 (2021) 451–462, https://doi.org/10.1016/j.carbon.2020.12.047.

[25] M. Dong, et al., Simultaneous enhancement of powder properties, additive manufacturability, and mechanical performance of Ti–6Al–4V alloy by 2D-nano-carbon decoration, Mater. Sci. Eng. A 859 (2022) 144215, https://doi.org/10.1016/j.msea.2022.144215.

[26] W. Xu, et al., Additive manufacturing of strong and ductile Ti–6Al–4V by selective laser melting via in situ martensite decomposition, Acta Mater 85 (2015) 74–84, https://doi.org/10.1016/j.actamat.2014.11.028.

[27] R. Magana-Carranza, et al., The effect of processing parameters and material properties on residual forces induced in Laser Powder Bed Fusion (L-PBF), Addit. Manuf 46 (2021) 102192, https://doi.org/10.1016/j.addma.2021.102192.

[28] A. du Plessis, Effects of process parameters on porosity in laser powder bed fusion revealed by X-ray tomography, Addit. Manuf. 30 (2019) 100871, https://doi.org/10.1016/j.addma.2019.100871.

[29] C. Zhao, et al., Critical instability at moving keyhole tip generates porosity in laser melting, Science 370 (6520) (2020) 1080–1086, https://doi.org/10.1126/science.abd1587.

[30] M. Yan, et al., Impacts of trace carbon on the microstructure of as-sintered biomedical Ti–15Mo alloy and reassessment of the maximum carbon limit, Acta biomater 10 (2) (2014) 1014–1023, https://doi.org/10.1016/j.actbio.2013.10.034.

[31] Y. Zhou, et al., Microstructuring of graphene oxide nanosheets using direct laser writing, Adv. Mater. 22 (1) (2010) 67–71, https://doi.org/10.1002/adma.200901942.

[32] A. Szkliniarz, W. Szkliniarz, Carbon in commercially pure titanium, Materials (Basel) 16 (2) (2023) 711, https://doi.org/10.3390/ma16020711.

[33] Y. Zhang, et al., Microstructure and mechanical property of MXene-Added Ti–6Al–4V alloy fabricated by laser powder bed fusion, Mater. Trans. 64 (6) (2023) 1169–1174, https://doi.org/10.2320/matertrans.MT-ME2022009.

[34] K. Shitara, et al., First-principles design and experimental validation of β-Ti alloys with high solid-solution strengthening and low elasticities, Mater. Sci. Eng. A 843 (2022) 143053, https://doi.org/10.1016/j.msea.2022.143053.

[35] L. Zhang, et al., Manufacture by selective laser melting and mechanical behavior of a biomedical Ti–24Nb–4Zr–8Sn alloy, Scripta Mater 65 (1) (2011) 21, https://doi.org/10.1016/j.scriptamat.2011.03.024. -24.

[36] S. Zhang, et al., Fatigue properties of a multifunctional titanium alloy exhibiting nonlinear elastic deformation behavior, Scripta Mater 60 (8) (2009) 733–736, https://doi.org/10.1016/j.scriptamat.2009.01.007.

[37] S. Li, et al., Fatigue properties of a metastable β-type titanium alloy with reversible phase transformation, Acta biomater 4 (2) (2008) 305–317, https://doi.org/10.1016/j.actbio.2007.09.009.

[38] C. Yang, et al., Simultaneous improvement in strength and plasticity of Ti-24Nb-4Zr-8Sn manufactured by selective laser melting, Mater. Des. 157 (2018) 52–59, https://doi.org/10.1016/j.matdes.2018.07.036.

[39] L. Yan, et al., Improved mechanical properties of the new Ti-15Ta-xZr alloys fabricated by selective laser melting for biomedical application, J. Alloys Compd. 688 (2016) 156–162, https://doi.org/10.1016/j.jallcom.2016.07.002.

[40] L. Elias, et al., Microstructural and mechanical characterization of biomedical Ti–Nb–Zr(–Ta) alloys, Mater. Sci. Eng. A 432 (1–2) (2006) 108–112, https://doi.org/10.1016/j.msea.2006.06.013.

[41] W. Chen, et al., Controlling the microstructure and mechanical properties of a metastable β titanium alloy by selective laser melting, Mater. Sci. Eng. A 726 (2018) 240–250, https://doi.org/10.1016/j.msea.2018.04.087.

[42] E. Bertrand, et al., Synthesis and characterisation of a new superelastic Ti–25Ta–25Nb biomedical alloy, J. Mech. Behav. Biomed. Mater. 3 (8) (2010) 559–564, https://doi.org/10.1016/j.jmbbm.2010.06.007.

[43] H. Liu, et al., Improved fatigue properties with maintaining low Young's modulus achieved in biomedical beta-type titanium alloy by oxygen addition, Mater. Sci. Eng. A 704 (2017) 10–17, https://doi.org/10.1016/j.msea.2017.07.078.

[44] S.L. Sing, et al., Selective laser melting of titanium alloy with 50 wt% tantalum: microstructure and mechanical properties, J. Alloys Compd. 660 (2016) 461–470, https://doi.org/10.1016/j.jallcom.2015.11.141.

[45] K. Pałka, R. Pokrowiecki, Porous titanium implants: a review, Adv. Eng. Mater. 20 (5) (2018) 1700648, https://doi.org/10.1002/adem.201700648.

[46] M.A. El-Sayed, Design optimization of additively manufactured titanium lattice structures for biomedical implants, Int. J. Adv. Manuf. Technol. 110 (2020) 2257–2268, https://doi.org/10.1007/s00170-020-05982-8.

[47] M. Das, et al., Tribological, electrochemical and in vitro biocompatibility properties of SiC reinforced composite coatings, Mater. Des. 95 (2016) 510–517, https://doi.org/10.1016/j.matdes.2016.01.143.